Phys. Status Solidi A **206**, No. 1, 106–115 (2009) / **DOI** 10.1002/pssa.200824403

physica status solidi a
www.pss-a.com
applications and materials science

Electrical resistivity and photoluminescence of zinc oxide films prepared by ultrasonic spray pyrolysis

Khedidja Bouzid[1], Abdelkader Djelloul[*,2], Noureddine Bouzid[3], and Jamal Bougdira[4]

[1] Laboratoire de microstructures et défauts dans les matériaux, Université de Constantine, Algérie
[2] LASPI[2]A Laboratoire des Structures, Propriétés et Interactions Inter Atomiques, Centre Universitaire Khenchela, Algérie
[3] Laboratoire de physique des matériaux, Université de Ouargla, Algérie
[4] LPMIA Laboratoire de Physique des Milieux Ionisés et Applications, Université Henri Poincaré Nancy, France

Received 24 June 2008, revised 23 September 2008, accepted 29 September 2008
Published online 4 November 2008

PACS 71.55.Gs, 78.20.Ci, 78.30.Fs, 78.55.Et, 78.55.Mb, 81.15.Rs

[*] Corresponding author: e-mail djelloulabdelkader@yahoo.fr, Fax: +213 32 33 19 60

Zinc oxide (ZnO) thin films have been prepared by ultrasonic Spray pyrolysis (USP) technique using zinc acetate dihydrate dissolved in methanol, ethanol and deionized water. A number of techniques, including X-ray diffraction (XRD), scanning electron microscopy (SEM), Fourier transform infrared (FTIR) spectroscopy, UV–visible, electrical resistivity, and photoluminescence (PL) were used to characterize the obtained ZnO thin films. The evolution of the preferred crystalline orientations in the ZnO films was systematically investigated. The PL measurements indicated that the as-grown ZnO thin films showed UV and green emission bands when they were excited by a Hg arc lamp using 313 nm as the excitation source. A red-shift in the near band edge (NBE) has been observed with the increase in the substrate temperature and has been attributed to the compressive intrinsic stress present in the films. It is confirmed that oxygen vacancy (V_O) is the most important factor that causes the broad visible emission. Furthermore, the visible emission and electrical resistivity of ZnO thin films are found to be a function of porosity. Also, it has been interestingly found that the intensity of green emission at ~2.5 eV remarkably increased when the obtained ZnO films were deposited at 320 °C. The reason might be the V_O, intrinsic stress, surface-to-volume ratio and porosity in the sample increased at low substrate temperature. The resistivity follows the same behavior as the intensity of the green emission. We propose a new luminescence mechanism based on the recombination related to oxygen vacancies in Zn-rich or stoichiometric conditions.

1 Introduction ZnO is amongst the most widely studied of all metal oxide systems and has recently become a very popular material due to its great potential for optoelectronics applications. The wide direct band gap of 3.3 eV and large exciton binding energy ~60 meV at room temperature [1] is especially attractive for optoelectronic, nonlinear optics and electro-optics applications [2]. Moreover, the binding energy of the exciton of ZnO (60 meV) is larger than its competitor GaN (25 meV) at room temperature making it attractive for exciton-related device applications [3], a dye-sensitized oxide semiconductor solar cell [4], and lasing devices operating at high temperatures and in harsh environments [5]. ZnO, in general, is an n-type material, with a high electrical conductivity due to lack of oxidation. The electrical properties of ZnO are closely related to the composition and the microstructure. It has been reported that the PL properties of ZnO are strongly dependent on the growth conditions including growth temperature and growth ambient [6]. Thus, the dominant defects for the visible emission might be different for samples grown by various techniques, and great care has to be taken when comparing the PL of samples prepared by various growth techniques. Previous research has shown that the PL spectrum of ZnO is sensitive to the particle shape, size, temperature, preparation method, etc. [7]. The emission by excitons was concluded as an origin of UV emission in ZnO thin films [8, 9]. Stoichiometric ZnO thin films usually show strong UV luminescence. However, the

exact origin of green emission is still in dispute, although defects such as oxygen vacancies, oxygen interstitials, zinc vacancies, zinc interstitials and oxide antisites are suggested as an origin of green PL by other groups [10–13]. Many authors explored the green luminescence mechanism of ZnO by combining PL, optical absorption and electron paramagnetic resonance (EPR) spectrum. Their results showed that the green luminescence is induced by the singly ionized oxygen vacancies in the form of F^+ centers [14, 15]. The study of the EPR spectrum of F^+ centers in the ZnO single-crystal indicates that the oxygen vacancy V_O in the system can be neutral, and represents a deep donor with the ionization energy equal to 2.73 eV [16]. Such centers are not responsible of the high electrical conductivity of ZnO, but are entirely able to radiate the light at 510 nm [17]. In this regard, the study of the PL characteristics of ZnO is interesting because it can provide valuable information on the quality and purity of the materials.

The aim of this paper is to bring a contribution in this field, based on some of our experimental results, from which some specific aspects of the growth processes can be extracted and discussed. In this respect we investigated the effects of structure and morphology on the PL and electrical resistivity of undoped ZnO thin films deposited by USP technique.

2 Experimental details The solution used for the films investigated here had the following amounts: 2.2 g $Zn(CH_3COO)_2 \cdot 2H_2O$ (Fulka 99.9%); 50 ml H_2O (deionized); 40 ml CH_3OH (Merck 99.5%); 60 ml C_2H_5OH (Merck 99.5%). A small amount of acetic acid was added to aqueous solutions to adjust the pH value to about 4.8 to prevent the formation of hydroxides. Water is the most convenient oxidizing agent. Methanol and ethanol were the obvious choice because of their volatility and thus facilitating quick transformation of the precursor mist into vapor form, which is an important criterion for obtaining good quality films.

The ultrasonic spraying system used in this work consists of a commercial ultrasonic atomizer VCX 134 AT and substrate holder with heater. The ultrasonic vibrator frequency was 40 kHz and the power used was 130 W. The median drop size at 40 kHz is 45 microns. The nozzle to substrate distance was 5 cm and during the deposition, the solution flow rate was held constant at 0.1 ml/min. Our equipment can be divided in three parts connected between them. One flask containing the zinc acetate solution, a perfusion system (a dropper chamber and a valve which regulates the dripping speed) and finally an ultrasonic atomizer (ultrasonic power supply, piezoelectric transducer and nozzle) located at 0.5 m under the level of flask. The zinc acetate solution is dispensed to the nozzle by gravity. To conserve the spray flow rate magnitude, the height of liquid was maintained constant by adding solution quantities, constantly, during deposition. The starting solution travels through the probe, and spreads out as a thin film on the atomizing surface. The oscillations at the tip disintegrate the liquid into micro-droplets, and then eject them to form a dense stream. Because the velocity of the droplets generated is very low, the probe is mounted with the tip facing downward in the direction of the substrate, and air disturbances kept to a minimum.

ZnO thin films were deposited onto microscope cover glass substrates ($30 \times 12 \times 1.2$ mm^3) in the temperature range: 320–420 °C and the deposition time was fixed at 30 min for all films. The substrate temperature was monitored with a thermocouple and controlled electronically. The film morphology was examined using a (Tescan Vega TS5130MM) scanning electron microscope (SEM). The structural analysis of the ZnO thin films is done by powder X-ray diffraction (XRD) data collected on Seifert XRD 3003-TT diffractometer using Cu K_α radiation. The transmittances of ZnO thin films were measured using a SpectroScan 80D UV–vis spectrophotometer in the 190–1100 nm spectral range. The infrared absorption modes of these films were obtained from FTIR absorbance measurements taken at room temperature using constant powder samples (40 μg) imbedded in 23 mg CsBr pellet of 5 mm diameter. The sample for FTIR measurement was prepared by grinding the thin film scraped from the glass substrate in a synthetic sapphire mortar and pestle and tabletting the ground solid with CsBr. The FTIR is performed with a Perkin–Elmer spectrometer with resolution of 8 cm^{-1}. The apparatus is equipped with a system allowing the reduction of the optical course in air in order to minimize the perturbations associated with ambient air (water vapour and CO_2). The uncertainty on the position of the various peaks is equal to ±2 cm^{-1}. For the electrical measurements two gold electrodes were deposited on the film by sputtering. Two platinum wires were applied on the electrodes and connected to a current–voltage generator (Keithley 237). PL measurement was carried out on a luminescence spectrometer (Perkin–Elmer LS-55B, Perkin–Elmer Instrument, USA) using a Hg arc lamp as the excitation source at room temperature. The excitation wavelength used in PL measurement was 313 nm.

3 Results and discussions

3.1 Structure and morphology Before discussing the PL and electrical resistivity of the thin films in more detail, it is useful to consider their crystal structure and morphology. X-ray diffraction analysis, obtained for 2θ scans between 20° and 70°, indicated that the deposited ZnO films on the glass substrate were polycrystalline and retained a hexagonal structure type wurtzite. The diffraction peaks are easily indexed on the basis of the hexagonal structure of ZnO ($P6_3m/c$, $a = 3.249$ Å, and $c = 5.205$ Å, JCPDS 36-1451). To better understand the decomposition process during USP, a set of samples were deposited at temperatures between 320 °C and 420 °C. In order to explore the dependence of structural properties on the substrate temperature, we investigated the changes in structural characteristics such as the crystal structure and surface morphology by means of XRD and SEM. Figure 1

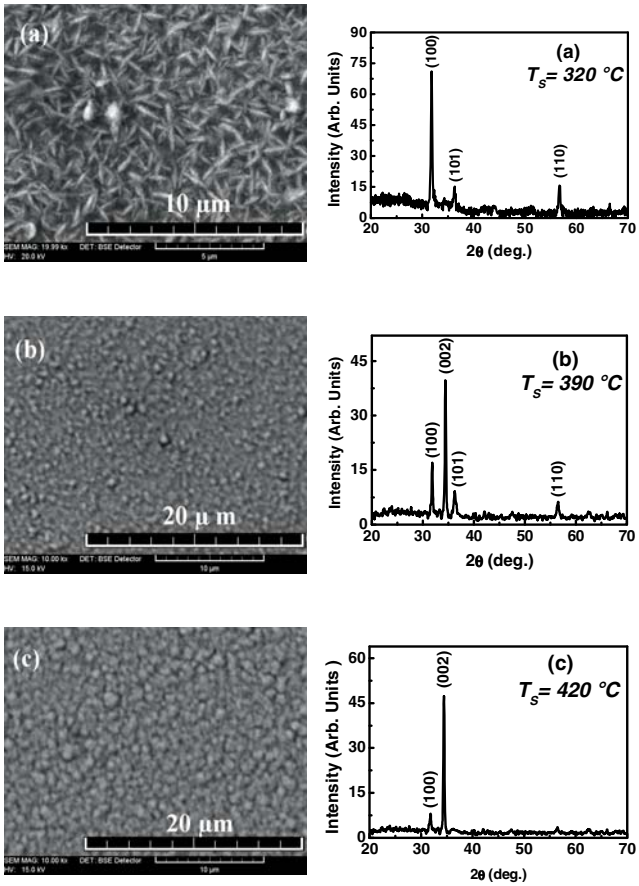

Figure 1 X-ray diffraction (XRD) and secondary electron micrographs (SEM) of ZnO films obtained from zinc acetate dihydrate solution by USP technique on glass substrate: (a) T_S = 320 °C; (b) T_S = 390 °C; and (c) T_S = 420 °C.

shows XRD patterns and SEM micrographs of ZnO films. Miller indices are indicated on each diffraction peak. It can be seen that a set of peaks with strong intensity can be indexed in peak positions to a crystalline ZnO phase. The results show that the thin films grown at T_S = 320 °C is crystalline since diffraction peak appears in the spectrum corresponding to the strong (100) and weak planes of the ZnO phase (Fig. 1(a)). Raising Ts changed preferred orientations from (100) to (002) with an intermediate stage which is powder like structure. It is clear from the Fig. 1(b) and (c) that as T_S is increased the thin films adopts a preferred orientation, with the *c*-axis (002) perpendicular to the substrate. These films show different morphology of surface grains, which are dependent on the deposition temperature. Though the films are all visually alike, i.e. mirror smooth, the nature of their morphology is quite different. Namely, the geometry of the aggregates grown at lower temperatures appears to be lenticular-like grains, whereas those grown at higher temperatures (>390 °C) become circular grains. The observation agrees with what is detected from the data of X-ray analysis, as shown by the diffraction spectra. The increasing of the substrate temperature is likely to drive the modification of the grain boundary configuration. It is well-known that the shape and size of inorganic functional materials have an important influence on their electrical and optical properties [18].

The crystallite size (D) of the samples was estimated using the Scherrer formula [19]

$$D = \frac{0.94\lambda}{B_{(hkl)} \cos\theta_{(hkl)}}$$

where λ, $\theta_{(hkl)}$ and $B_{(hkl)}$ were the X-ray wavelength (1.54056 Å), Bragg diffraction angle and line width at half-maximum, respectively. The values of $B_{(hkl)}$ and $\theta_{(hkl)}$ parameters from the XRD peak are estimated by Gaussian fitting. This formula is not limited by the preferential orientation and is valid for an ordinary XRD profile. We choose the (100) diffraction peak for sample (a) and (002) peak for samples (b) and (c) to calculate the crystallite sizes since they are prominent in the involved profiles. The crystallite sizes of the films deposited on glass substrate at T_S = 320 °C, 390 °C and 420 °C was found to be 30 nm, 37 nm and 40 nm, respectively. The mean crystallite size obtained using Scherrer's formula are all case substantially smaller than the dimension of grains observed by SEM image, indicating these grains are probably an aggregation of many crystallites.

3.2 Fourier transform infrared (FTIR) analysis

FTIR spectroscopy supplements the information obtained from XRD and SEM. It is the combination of all data helps us to understand, analyze and refine more effectively the structure of films. Figure 2 shows the FTIR absorbance spectra of ZnO samples grown at different substrate temperatures: (a) T_S = 320 °C, (b) T_S = 390 °C and (c) T_S = 420 °C measured at room temperature, together with that of bulk ZnO and zinc acetate dihydrate for comparison. Here, signal derived from glass substrate was never detected in this measurement because the measurement was performed with the solid scraped from the substrate. Thus, the peak position of Zn–O vibration frequency shifts relative to the single crystal value (437 cm^{-1}) can be used to estimate intrinsic stress in ZnO samples.

The FTIR spectrum illustrates a series of absorption bands in the range of 200–4000 cm^{-1}. This spectral region encompasses several important stretch modes involving carbon bonded to hydrogen as well as to oxygen, hydrogen bonded to oxygen and bonding between Zn–O (448 cm^{-1} (a), 441 cm^{-1} (b) and 440 cm^{-1} (c)) are clearly represented, and significant up-shift as compared with that of bulk ZnO French process (437.33 cm^{-1}). The broad asymmetrical absorption region that peaks around 3440 cm^{-1} is likely due to the OH stretching mode of hydroxyl group. Theoretical calculations predict O–H vibrations in ZnO ranging from 3216 cm^{-1} to 3644 cm^{-1}, depending on the configuration and number of hydrogen atoms in the complex [20]. The hydroxyl results from the hygroscopic nature of ZnO. Three peaks of very weak intensities at 2856 cm^{-1}, 2927 cm^{-1}

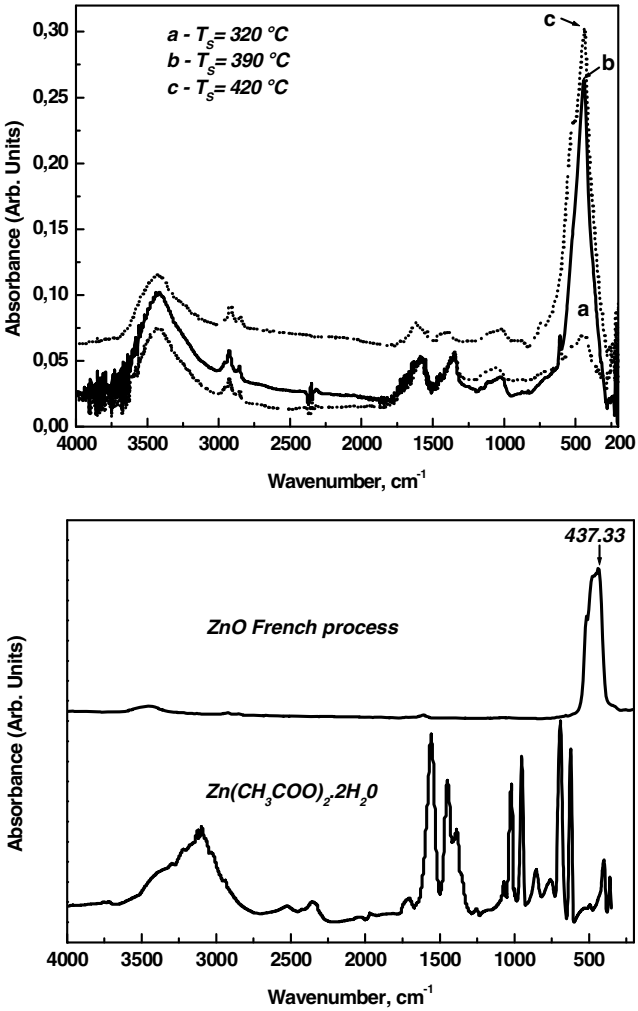

Figure 2 FTIR absorption spectra of ZnO samples deposited at (a) $T_S = 320$ °C, (b) $T_S = 390$ °C and (c) $T_S = 420$ °C, (top), together with that of bulk ZnO and zinc acetate dihydrate powder for comparison (bottom). The main bands are discussed in the text.

and 2960 cm^{-1} are observed which are due to C–H stretching vibrations of alkane groups. These specific peaks correlate well with the observed frequencies of the C–H_2 symmetric stretch (2855 ± 10 cm^{-1}), C–H_2 asymmetric stretch (2926 ± 10 cm^{-1}), and C–H_3 asymmetric stretch (2962 ± 10 cm^{-1}) of saturated hydrocarbons, respectively [21–24]. The peaks observed at 1350 cm^{-1} and 1582 cm^{-1} are due to the asymmetrical and symmetrical stretching of the zinc carboxylate (–COO^-), respectively [25]. According to the literature, a unidentate or monodentate acetate ligand usually lies around $\Delta\nu \geq 200$ cm^{-1}, the frequency separation of a bidentate ligand lies between 80–160 cm^{-1}, in which the bridging acetate usually has a larger $\Delta\nu$ of 120–160 cm^{-1} [26]. Nevertheless, these bands are clearly shifted compared to those displayed for the bidentate acetate ligand in $Zn(CH_3COO)_2 \cdot 2H_2O$ [27]. Figure 2 compares the infrared wavelength range for the ZnO samples and zinc acetate dihydrate powder. The average separation of these two bands, $\Delta\nu = 232$ cm^{-1} is typical of unidentate acetate ligand ($\Delta\nu = 110$ cm^{-1} for zinc acetate dihydrate). This confirms that acetate is complexed with metal zinc, likely in the surface. The small peak at 1040 cm^{-1} represents C=O deformation. The absorption in ~2359 cm^{-1} is due to the presence of CO_2 molecular in air. The FTIR results strongly support the hypothesis that at least some of the carbon and hydrogen co-exist as defect complexes in the undoped ZnO and their absorption bands have no obvious change. As can be seen from the peak intensity of the Zn–O bond increased with an increasing growth temperature. This was also strong evidence that the thin films grown at 420 °C had the best crystal quality. Combined this with our XRD analyses results, we believe that in our USP-fabricated ZnO films, a large fraction of carbon is present in the form of CH_x ($x = 2$, and 3) and –COO^- defect complexes. These complexes most likely come from metalorganic precursors. Together these suggest that the FTIR-identified impurities exist mainly near crystallite surfaces.

The origin of the residual stress in the as-deposited ZnO/glass film can be realized as the followings: it is known that the residual stress in ZnO films contains a thermal stress component and an intrinsic stress component [28]. Intrinsic stress has its origin in the imperfection of the crystallites during growth. Several growth parameters, such as deposition temperature, deposition pressure and gas mixture would contribute to the intrinsic stress. The classic model of Pilling and Bedworth explains the stresses induced by oxide growth [29]. In this model, the tensile or compressive stresses are related to a change in volume, as the metal is converted into oxide. The ratio of the volume per metal ion in the oxide to the volume per metal atom in the metal has commonly been termed PBR, the Pilling–Bedworth ratio. The PBR can be calculated using the following equation:

$$\mathrm{PBR} = \frac{\rho_{\mathrm{M}} M_{\mathrm{M}_x\mathrm{O}_y}}{x m_{\mathrm{M}} \rho_{\mathrm{M}_x\mathrm{O}_y}},$$

where M_{MO} is the molecular weight of the oxide, m_{M} the atomic weight of the metal, ρ_{MO} the density of the oxide, ρ_{M} the density of the metal, and x the number of oxygen per the metal molecule. Compressive stresses are developed in the oxide when PBR > 1 and tensile stresses are developed when PBR < 1. The PBR for Zn/ZnO is 1.58. As a consequence; compressive stresses are present in the ZnO layer. FTIR and Raman spectroscopy both involve IR wavelength radiation and both measure the vibrational energies of molecules but these methods rely only on different selection rules. The frequency shift of the E_2 (high) is attributed to the stress variation. The compressive stress can be calculated from the shift in E_2 from [30]

$$\Delta\omega = \omega_{\mathrm{sample}} - \omega_{\mathrm{ref}} = -K\sigma,$$

where ω_{sample} and ω_{ref} (= 437 cm^{-1}) are the wavenumber peak position of the stressed and unstressed samples, σ is

the intrinsic stress in GPa and K is a constant. The pressure dependence of the high frequency nonpolar optical phonon E_2 mode in ZnO wurtzite phase (K) is 5.2 cm^{-1} GPa^{-1} as determined by Mitra et al. [31]. Based upon this result, the residual intrinsic compressive stress component for all ZnO films deposited in this work is estimated to be on the order of 0.576–2.115 GPa. When the crystallization is completed at high temperature, it results in the decrease of residual intrinsic stress in the ZnO films. The lattice strain in these films can be modified through deposition temperature.

3.3 Optical and electrical studies Gases like CH_3COOH, H_2O, etc. were produced as $Zn(CH_3COO)_2$ was oxidized into ZnO. Consequently, pores were easily formed due to the release of these gases. The porosity P is calculated from optical constants using the Lorentz–Lorenz equation [32]:

$$P = 1 - \frac{\left(n_{\text{film}}^2 - 1\right)\left(n_{\text{bulk}}^2 + 2\right)}{\left(n_{\text{film}}^2 + 2\right)\left(n_{\text{bulk}}^2 - 1\right)}, \quad (1)$$

where n_{film} is the refractive indices of the porous ZnO films and n_{bulk} is the refractive indices of the ZnO skeleton which is widely accepted as 2.008 at λ = 632 nm [33, 34]. To calculate the refractive index, n_{film}, the method suggested by Swanepoel was used [35, 36]. The optical parameters are obtained by using only the transmission spectrum. The spectral dependence of the transmittance, T, of ZnO thin films deposited on the glass substrate was measured in the wavelength range of 190–1100 nm. The data is illustrated in Fig. 3. The spectrum shows interference pattern with a sharp fall of transmittance at the band edge. The method used to calculate the refractive index is based on the approach of Manifacier et al. [37] who suggested creating an upper and lower envelope of the transmission spectrum beyond the absorption edge. The refractive index in the region, where α approaches zero is given as [38]

$$n_{\text{film}} = [M + (M^2 - s^2)^{1/2}]^{1/2}, \quad (2)$$

where

$$M = 2s\frac{T_{\max} - T_{\min}}{T_{\max}T_{\min}} + \frac{(s^2 + 1)}{2}. \quad (3)$$

Here s is the refractive index of substrate, which is typically 1.52 for the totally transparent glass substrate used in this study. $T_{\max}$ and $T_{\min}$ are the values of the envelope at the wavelengths in which the upper and lower envelopes and the experimental transmittance spectrum are tangent, respectively. Refractive index can be estimated by extrapolating the envelops corresponding to $T_{\max}$ and $T_{\min}$. All the ZnO films are highly transparent in the visible region 400 nm to 1100 nm and a sharp fall in transmittance is observed below 400 nm due to band gap absorption (Fig. 3). Therefore, an average transmittance value in the region 430 nm to 1100 nm is calculated from the transmission spectra and substituting the value in Eq. (3), n_{film} value of the film is obtained. The calculated values of the refractive index from transmission spectrum at the wavelength of 632 nm are plotted in inset of Fig. 4 and are in good agreement with the results obtained by other groups [39, 40]. The refractive indices of the sample grown at the temperatures higher than 350 °C at λ = 632 nm are in the reasonable range of 1.81–1.91 compared with that of single crystalline ZnO. However, the refractive indices of the samples grown at the temperatures lower than 350 °C are a little smaller than the normal values suggesting the presence of a higher void content in the latter films. The reason for this phenomenon is from the poor qualities of the films deposited at low temperatures. The density of such film is also smaller than that deposited at higher temperatures. Next, the average porosity of each film has been calculated using the Eq. (1). The porosity of the ZnO films is represented in Fig. 4 as a function of substrate temperature. Obviously, the porosity decreased considerably with substrate temperature until 390 °C and then decreased slowly until 420 °C.

With the increase of the substrate temperature the electrical resistivity of ZnO films deposited on the glass substrates decreases. The crystallinity of films was enhanced with increasing the deposit temperature as shown in Figs. 1 and 2 and in addition, the grain boundary density decreased due to the growth and agglomeration of grains, which indicated that the grain boundary scattering of carriers decreased. It is important to mention that the morphology in addition to the porosity of the films and the crystalline structure could be related to the electrical conduction behavior. The strong reduction of resistivity from 7.1×10^3 to 51 Ω cm as the deposition temperature of undoped samples increases from 320 °C to 420 °C is followed by an increase of the film density (from 4.59 g cm^{-3} to 5.32 g cm^{-3}, the theoretical density of ZnO = 5.675 g cm^{-3}), different morphology of surface grains, change of orientation of

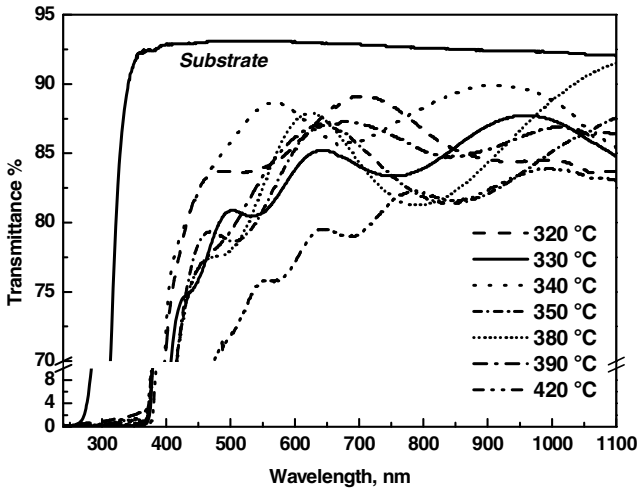

Figure 3 Transmission spectra of ZnO thin films deposited by USP technique on glass substrate at different T_S.

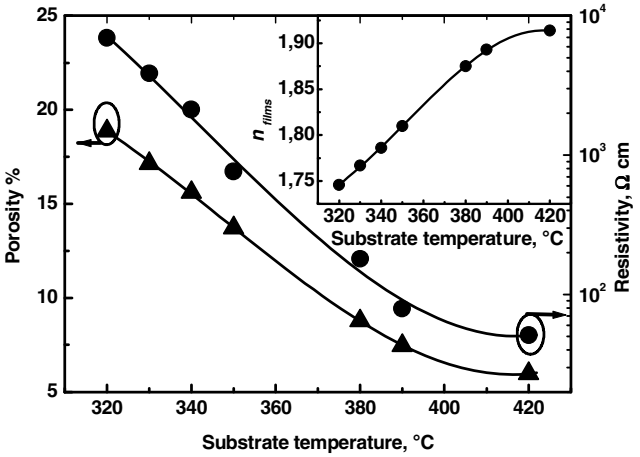

Figure 4 Electrical resistivity and porosity of ZnO thin films deposited on glass substrate at different T_S. The inset shows refractive index at 632 nm of the ZnO thin films as a function of substrate temperature.

hexagonal grains, which becomes parallel to the substrate and strain/stress relaxation in larger crystallite size. To interpret the conductivity behavior of ZnO thin films, we can assume that the resistivity of these films comes from the sum of resistivities of the grain boundary, lattice, impurity, strain and porosity. The grain boundary barrier depends on the microvoids, inter-grain distance, grain size, impurity concentration, crystallinity, and non coordinated atoms at the grain boundaries [40]. The contribution of grain boundary region to the electronic properties increases as the grains become smaller; there are large number of grains and hence large area of the grain surface, which resulted in higher resistivity of the thin films. Lattice contribution is expected through the interreticular spacing (d) and intrinsic stress. From the Figs. 4 and 1, we can see that all ZnO films with resistivity less than 140 Ω cm have relatively small d spacing ($d_{(002)} = 0.26$ nm), while the poorly conductive ZnO films (samples with resistivity $>10^3$ Ω cm) have a larger d spacing ($d_{(100)} = 0.28$ nm). The compressed lattice is expected to provide a wider band gap because of the increased repulsion between the oxygen 2p and the zinc 4s bands [41]. The electrical resistivity of the films increases exponentially with increasing strain. The results also show that the poorer conducting films have higher porosity (density <4.86 g cm^{-3}), while the most conductive ZnO films have lower porosity (density >5.26 g cm^{-3}). This enhancement of density and inter-grain contacts leads to lower resistivity. The high resistivity value observed can be attributed, at least partly, to the porosity of the films. A decrease in the room-temperature resistivity with increasing substrate temperature is attributed mainly to the increase of grain size as well as the partial decrease of the porosity, while an increase in the resistivity with decreasing T_S, when porosity was greater, is due to the increase of the electrical barrier height of grain boundaries. Further, the excess resistivity is consistent with the argument of Tokumoto et al. [42] that a missorientation of lenticular-like

Table 1 Characteristics of the ZnO samples estimated from XRD patterns, FTIR, transmission spectra and resistivity measurements.

sample	(a)	(b)	(c)
substrate temperature (°C)	320	390	420
crystallite size (nm)	30	37	40
Zn–O bond (cm^{-1}), ω_{sample}	448	441	440
intrinsic stress (GPa)	–2.115	–0.769	–0.576
transmittance (%) at $\lambda = 623$ nm	87	86	80
refractive index at $\lambda = 623$ nm	1.74	1.90	1.91
porosity (%)	19.0	9.0	5.9
resistivity (Ω cm)	7100	79	51

grains, meanly edge-to-edge or edge-to-face bounded, observed for the film deposited at 320 °C (Fig. 1(a)) is the main reason responsible for its high resistivity. In addition, with the increase of porosity, the contact between individual grains looked more dispersed. The considerable separation between grains and the reduced grain boundary area lead to few continuous electrical conductive ways, resulting in low macroscopic conductivity. Because porosity is inversely proportional to grain size, resistivity decreased with the increased of grain size accordingly. In addition to the decrease of porosity, a more complete pyrolysis of starting precursors is achieved at the highest deposition temperature, and this would yield a film in which the carbon compound content is minimal so favouring a higher electrical conductivity [43]. Characteristics of the ZnO samples estimated from XRD patterns, FTIR, Transmission spectra and resistivity measurements are summarised in Table 1.

3.4 Room temperature photoluminescence analysis The band-to-band excitation of ZnO promotes electrons from the valence band to the conduction band, leaving holes in the valence band. The holes migrate from the valence band to deep levels and recombination occurs between electrons from either the conduction band or shallow donor levels and trapped holes on deep levels [44]. Basically the PL of ZnO is related to the presence of holes in the valence band. Room temperature PL spectra of the ZnO thin films measured using an Hg lamp of 313 nm as excitation source is shown in Fig. 5. Two luminescence bands are observed. One is a relative weak and narrow UV emission peaking at about (a): 3.25 eV, (b): 3.16 eV, (c): 3.12 eV corresponds to the NBE emission, which is responsible for the recombination of the free excitons of ZnO [45]. Another is a strong and broad green emission band centered at (a): 2.52 eV, (b): 2.48 eV, (c): 2.45 eV, which may originate from the commonly assumed the recombination of the photoexcited holes with the electrons occupying the singly ionized oxygen vacancies [46].

As shown in the figure, both samples (a) and (b) exhibit very strong, broad green-light and weak UV emission, while sample (c) has strong UV and weak green emission. The green-peak near 2.47 ± 0.05 eV is a widely observed

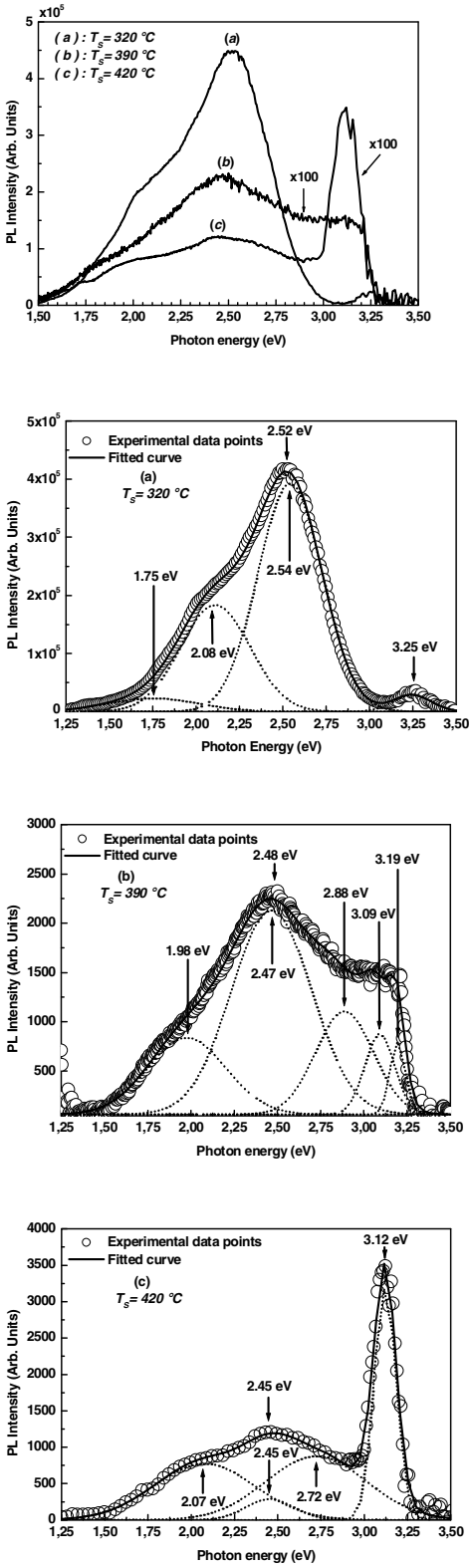

Figure 5 PL spectra of the ZnO thin films grown at different substrate temperatures: (a) $T_S = 320$ °C, (b) $T_S = 390$ °C and (c) $T_S = 420$ °C measured at room temperature. Gaussian deconvolution components (dashed lines) and the fit to the data (thin solid line) are shown.

defect related emission in ZnO [47]. It is well understood that PL spectra depend on the stoichiometry and the microstructure of the films. ZnO is nonstoichiometric oxide containing oxygen vacancy (V_O) and reduced interstitial zinc species. These defects formed when the zinc acetate was transformed into ZnO in the USP process. Zinc acetate is a reductant whose decomposition to most stable compounds needs oxygen. ZnO is Zn-rich due to the rapid evaporation of water which is the source of oxygen in the growth process and the low concentration of oxygen in the air near the substrate according to the ideal gas law. In our work, the rapid evaporation-oxidation process, V_O should be generated because of partially incomplete oxidation and crystalline. In addition, the ZnO grain with high aspect ratio and lenticular-like morphology should also favour the existence of large quantities of V_O. The red color of our as-deposit ZnO thin films at 320 °C indicates the existence of the deep levels which make the sample absorb green and blue light. This means that ZnO, which formed by the pyrolysis of zinc acetate, has increasing density of V_O. Furthermore, the reason may be responsible for the compressive intrinsic stress is the lattice distortion caused by the V_O. The larger intrinsic stress (2.115 GPa) of sample deposited at $T_S = 320$ °C could be attributed to the more V_O defects in the thin films, which made the lattice more distorted, which testified the results of the PL spectrum (Fig. 6(a)). The lattice relaxations around V_O are large and very different in different charge states. For neutral oxygen vacancy ($V_O^{\times}$), the four Zn nearest neighbors are displaced inward by 12% of the equilibrium Zn–O bond length, whereas for singly ionized oxygen vacancy ($V_O^{\bullet}$) and doubly ionized oxygen vacancy ($V_O^{\bullet\bullet}$) the displacements are outward by +2% and +23% [48]. These facts again indicate that the visible luminescence bands from ZnO are associated with V_O in ZnO thin films. The intensity of the NBE emission increased with increasing growth temperature. The PL results coincided well with the structure change investigated by XRD. The intensities of UV emission band and visible one correlates with each other and depends on the crystallite size. As crystallite size increases the intensity of UV emission enhances meanwhile the deep level emission decreases. With the increased crystallite size and a decrease in the intrinsic stress of the ZnO films, a red-shift in the peak position of the PL band was observed.

When the balance between zinc and oxygen was reached and the defects due to the non-stoichiometry are minimized, the PL spectrum was almost free of visible emission. The absence of the deep level emission in PL spectrum indicates high material quality. The relative intensity of the defect peak at ~2.5 eV decreases slightly with substrate temperature, indicating the better crystalline quality of the samples deposited at higher substrate temperatures. This suggests that due to enough thermal energy supplied by increase of the growth temperature atoms move to stable sites and that impurities moved to grain boundary. Therefore the defect density of inside grain is

diminished and PL properties of ZnO films are improved. The mean crystallite size was ~40 nm for the sample deposited at T_S = 420 °C which was larger value as compared to all samples and is colorless transparent suggesting the deep level defects annihilate. We conclude that the films, which present strong PL intensity in UV emission, have a strong XRD intensity and large crystallite size, therefore a good crystallinity. It can be seen that the size of ZnO crystallites exhibits gradual increase with the increase of the deposition temperature, and the film deposited at T_S = 320 °C possesses the smallest crystallites (~30 nm). From the PL spectra, it can be seen that the intensity of the green emission for ZnO sample (a), with a porosity of 19%, is much stronger than the other two samples. The best green luminescent films possessed a porous structure and smallest crystallites [49]. For instance, the luminescence intensity at 2.52 eV of the sample (a) is approximately 370 times higher than that of the sample (c) measured under the same excitation conditions. Moreover, it has also been proposed that the green emission of ZnO nanowires increases with the surface to volume ratio increases [7]. Thus the ZnO sample (a) will also exhibit much intense green emission due to the larger surface area. As discussed above, with increase of substrate temperature, stoichiometric deviation of ZnO is improved and concentration of intrinsic defects such as oxygen vacancy decreases, leading to attenuation of the green band and enhancement of NBE emission.

By optimizing the peak position and half-width of the Gaussian peaks, it was possible to obtain a good fit for the multi-peak combination. The Gaussian peaks (dashed lines) are shown at the bottom of Fig. 5a–c, while the solid lines represent the linear combination of the multi-Gaussian peaks with a constant background. The peak positions are marked. Mathematic treatment of the PL spectra has shown that wide VIS-band consists of a series of overlapping bands. Five dominating bands are characterized by l.75, ~2.04, ~2.50, ~2.80 and ~3.09 eV. With the increased crystallite size of the ZnO films, a red-shift in the peak position of the PL band was observed. The peak position of NBE was varied from 3.25 eV ((a) in Fig. 5) to 3.12 eV ((c) in Fig. 5) and the red shift was about 130 meV. The full widths at half-maximum are 220 meV and 120 meV, respectively. Srikant et al. [50] by comparing measurements of the same crystals made by a variety of different techniques, it is concluded that the optical band gap of ZnO at room temperature is 3.3 eV. The reports of an apparent band gap at 3.1 eV and 3.2 eV are concluded to be due to the existence of a valence band-donor transition at 3.15 eV which can dominate the absorption spectrum when the bulk, as distinct from the surface, of a crystal is probed.

Compared with bulk ZnO, the visible emission is broadened and it can be deconvoluted into three bands, for each sample, centered at about 1.75 eV (sample (a)), 2.04 ± 0.04 eV (samples (a)–(c)), 2.50 ± 0.05 eV (samples (a)–(c)) and 2.80 ± 0.08 eV (samples (b) and (c)), respectively. The compressive stress causes an increase of the band gap. In this manner, the red emission at 1.75 eV (sample (a)) might form due to largest band gap. Usually the appearance of the bands with energy <1.77 eV follows with the sharp decrease of UV luminescence [51]. Thus the existence of the centers responsible for these bands results in the quenching the UV luminescence. The intensity of red emission at 1.75 eV is not very high and the quenching effect is pronounced rather weak and one can observe the UV band in the luminescence spectra. We speculate that the recombination process of red emission occurs between photo-generated holes bound at a deep-level state and free electrons in conduction band.

The deconvoluted peaks of the luminescence clearly exhibit broad emissions in the range of 1.25–2.75 eV centered at around 2.0 eV. This band exists in all spectra. This means that the defect responsible for the yellow luminescence is inherent in the growth process by the USP technique. Consequently, the yellow emission in our present work is associated with oxygen vacancies.

Vanheusden et al. [46] found that the intensity of the green luminescence ranging from 2.34 eV to 2.53 eV in ZnO correlates very well with the paramagnetic single ionized oxygen-vacancy density, by the electron-paramagnetic-resonance (EPR) measurements. Only the singled ionized state can give rise to the green emission. In addition, evidence is presented that V_O are behind the shift in the optical absorption band that produces the red coloration in ZnO under Zn-rich anneals. This shift was found to be in the average of 0.7 eV confirming the relatively deep donor nature of V_O [52]. It has been shown that the intensity of the green emission was strongly influenced by the surface condition. Through the surface band bending the chemisorbed oxygen played a crucial role in the recombination process of the green emission [53].

Based on this founding and our experimental results in Fig. 5, the $V_O^{\bullet}$ defects may be a source for the green emissions at 2.50 ± 0.05 eV in our case. The oxygen vacancies of ZnO can produce two defect donor levels, the deep level at 1.3–1.6 eV and the shallow level at 0.3–0.5 eV below the conduction band [54]. The energy difference between this latter level and the valence band is 2.8 eV, which is consistent with the photon energy of the blue emission observed in this study after the deconvolution results of PL spectra (sample (a) and (b)). Consequently, the blue emission at around 2.8 eV may be caused by the electron transition from the shallow donor level of an oxygen vacancy to the valence band. Violet emission from ZnO at around 3.00 eV has been previously reported from a sample prepared in an oxygen-deficient condition [55]. The electron transition from interface trap level, at the grain boundary of Zn films, to the valence band was considered to be the origin of the violet emission. In our investigation, the defect contents were characterized by FTIR spectroscopy. It was found that in our set of samples the dominated surface defects are hydroxyl, carboxylate, and alkane from acetate group. Compared with other types, the unidentate type of

acetate group was reported to be more capable of trapping photogenerated holes near the valence band [56]. Therefore the peak at 3.09 eV could be related to a defect level in the grain boundaries.

The porous ceramics are advantages to oxidize grain boundaries and to produce surface acceptor states [57]. This suggests that oxygen is adsorbed at the grain boundaries, thus significantly increasing the potential barrier height, which results from an increase of surface states density [58]. Because porosity is inversely proportional to grain size and potential barrier height decreases with the increased of grain size, therefore, the barrier height increases with the increased of porosity. Consequently, the porosity will cause the increase of oxygen absorption on surface under Hg excitation, which higher the surface potential and thus further increases the width of the depletion region. The surface depletion region will modify the types and relative numbers of the oxygen vacancies that can exist in a ZnO films. Meanwhile, when porosity was greater, barrier heights of ZnO grain surface were larger and thus the grain will be thoroughly depleted. All the $V_O^{\times}$ centers will be reduced of electrons and converted to $V_O^{\bullet}$ and $V_O^{\bullet\bullet}$, hence $V_O^{\times}$ related emission will not be observed from such films (sample (a)). In our experiment, the diameter of the measured ZnO crystallite of sample (a) is 30 nm and porosity of 19%, the grains are intensively depleted. Therefore, the green and yellow peaks can be observed obviously, but the blue peak is absent. As the porosity decreases to $\leq$7% and grain size becomes large, the width of the depletion region decreases, and the grain becomes partially depleted under Hg lamp illumination. Consequently, $V_O^{\times}$ can exist in non-depletion region, and all types of V_O related visible emissions can be observed (sample (b)). Excess of zinc during the growth was found to cause an appearance of the PL peak at around 2.8 eV, which indicates that the corresponding defects are predominantly formed under Zn-rich or stoichiometric conditions. Therefore, at $T_S = 420$ °C, only $V_O^{\bullet\bullet}$ centers in the depletion region ($V_O^{\bullet}$ present in negligible quantity) and $V_O^{\times}$ centers in the non-depletion region can serve as luminescence centers to emit yellow and blue light, respectively. In fact, these three transitions are involved in the different grain regions on account of the changes in defect chemistry [59]. Through the width variation of the depletion region and the modification of the types and relative numbers of oxygen vacancies, the visible emission of ZnO thin films is found to be a function of porosity. In single crystal ZnO, formed under stoichiometric conditions, without surface effect and porosity, only UV peaks is observed.

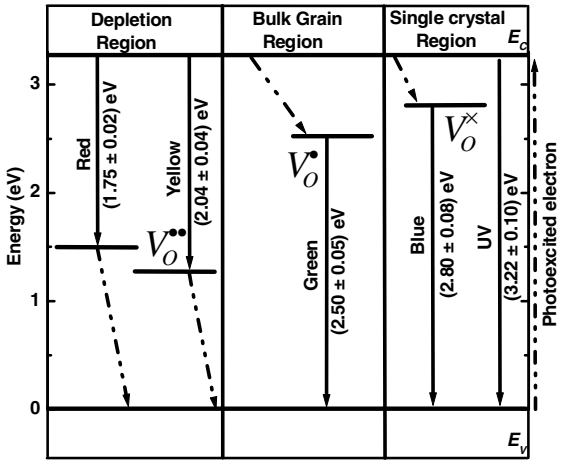

Figure 6 Scheme of the UV emission and the visible radiative emission processes.

Based on representative mechanisms of the green emission [49, 58–60], the discussed recombination models for the PL emission of ZnO thin films, deposited by USP technique (Zn-rich), are summarized in Fig. 6. This model allows us to better understand the mechanisms of transition from PL emission of ZnO grown under Zn-rich or stoichiometric conditions.

4 Conclusion In conclusion, undoped ZnO films were deposited by USP technique using zinc acetate dihydrate dissolved in methanol, ethanol and deionized water, within the substrate temperature range 320 °C–420 °C. It was seen that the orientation changed with a temperature increase. ZnO Films with different textures were obtained depending on the growth parameters. Specific preparation conditions to obtain films having the (100) or (002) orientation only were found. In this work, different PL spectra were observed by varying the substrate temperature. As the substrate temperature increased, the intensity of UV peak was increased while the intensity of the visible peak and the resistivity were decreased. It is confirmed that oxygen vacancies are the most important factor that causes the broad visible emission. Furthermore, the visible emission and electrical resistivity of ZnO thin films are found to be a function of V_O, intrinsic stress, surface-to-volume ratio and porosity. The degree of porosity could propose the mechanism of UV and visible luminescence and it will be used to control the optical properties of ZnO thin films for optical device applications.

References

[1] W. Y. Liang and A. D. Yoffe, Phys. Rev. Lett. **20**, 59 (1968).
[2] I. V. Kityk, J. Ebothe, A. Elchichou, M. Addou, A. Bougrine, and B. Sahraoui, Phys. Status Solidi B **234**, 553 (2002).
[3] F. K. Shan, B. C. Shin, S. C. Kim, and Y. S. Yu, J. Eur. Ceram. Soc. **24**, 1861 (2004).
[4] K. Hara, T. Horiguchi, T. Kinoshita, K. Sayama, H. Sugihara, and H. Arakawa, Sol. Energy Mater. Sol. Cells **64**, 115 (2000).
[5] T. Makino, C. H. Chia, T. T. Nguen, Y. Segawa, M. Kawasaki, A. Ohtomo, K. Tamura, and H. Koinuma, Appl. Phys. Lett. **77**, 1632 (2000).
[6] W. Jia, K. Monge, and F. Fernandez, Opt. Mater. **23**, 27 (2003).
[7] M. H. Huang, Y. Wu, H. Feick, N. Tran, E. Weber, and P. Yang, Adv. Mater. **13**, 113 (2001).

[8] K. I. Ogata, T. Kawanishi, K. Maejima, K. Sakurai, Shi. Fujita, and Shig. Fujita, Jpn. J. Appl. Phys. **40**, 657 (2001).
[9] Y. R. Ryu, S. Zhu, D. C. Look, J. M. Wrobel, H. M. Jeong, and H. W. White, J. Cryst. Growth **216**, 330 (2000).
[10] E. G. Bylander, J. Appl. Phys. **49**, 1188 (1978).
[11] K. Vanheusden, C. H. Seager, W. L. Warren, D. R. Tallant, and J. A. Voiget, Appl. Phys. Lett. **68**, 403 (1996).
[12] M. Liu, A. H. Kitai, and P. Mascher, J. Lumin. **54**, 35 (1992).
[13] B. Lin, Z. Fu, and Y. Jia, Appl. Phys. Lett. **79**, 943 (2001).
[14] G. Muller, Phys. Status Solidi B **76**, 525 (1976).
[15] F. A. Kröger and H. J. Vink, J. Chem. Phys. **22**, 250 (1954).
[16] V. Soriano and D. Galland, Phys. Status Solidi B **77**, 739 (1976).
[17] W. F. Wei, Phys. Rev. B **15**, 2250 (1977).
[18] Y. Zhang and Y. D. Li, J. Phys. Chem. B **108**, 17805 (2004).
[19] B. D. Cullity, Elements of X-Ray Diffraction, 2nd ed. (Addison-Wesley, Reading, MA, 1978), p. 102.
[20] E. V. Lavrov, J. Weber, F. Börrnert, C. G. Van de Walle, and R. Helbig, Phys. Rev. B **66**, 165205 (2002).
[21] N. B. Colthup, L. H. Daly, and S. E. Wiberly, Introduction to Infrared and Raman Spectroscopy, 3rd ed. (Academic Press, New York, 1990), p. 546.
[22] B. Smith, Infrared Spectral Interpretation, a Systematic Approach (CRC Press, Boca Raton, FL, 1999), p. 265.
[23] N. H. Nickel and K. Fleischer, Phys. Rev. Lett. **90**, 197402 (2003).
[24] G.-C. Yi and B. W. Wessels, Appl. Phys. Lett. **70**, 357 (1997).
[25] G. Socrates, Infrared and Raman Characteristic Group Frequencies, 3rd ed. (Wiley, New York, 2001), p. 347.
[26] K. Nakamoto, Infrared and Raman Spectra of Inorganic and Coordination Compounds (Wiley, New York, 1986), p. 231.
[27] S. Sakohara, M. Ishida, and M. A. Anderson, J. Phys. Chem. B **102**(50), 10169 (1998).
[28] W. Water and S. Y. Chu, Mater. Lett. **55**, 67 (2002).
[29] N. B. Pilling and R. E. Bedworth, J. Inst. Met. **29**, 529 (1923).
[30] I. de Wolf, Semicond. Sci. Technol. **11**, 139 (1996).
[31] S. S. Mitra, O. Brafman, W. B. Daniels, and R. K. Crawford, Phys. Rev. **186**(3), 942 (1969).
[32] M. R. Baklanov, K. P. Mogilnikov, V. G. Polovinkin, and F. N. Dultsev, J. Vac. Sci. Technol. B **18**, 1385 (2000).
[33] G. Wypych, Handbook of Fillers, 2nd ed. (Chem Tech Publishing, Canada, 1999), p. 172.
[34] F. K. Shan, G. X. Liu, W. J. Lee, G. H. Lee, I. S. Kim, B. C. Shin, and Y. C. Kim, J. Cryst. Growth **277**, 284 (2005).
[35] R. Swanepoel, J. Phys. E **17**, 896 (1984).
[36] R. Swanepoel, J. Phys. E **16**, 1214 (1983).
[37] J. C. Manifacier, J. Gasiot, and J. P. Fillard, J. Phys. E **9**, 1002 (1976).
[38] E. M. Bachari, G. Baud, S. Ben Amor, and M. Jacquet, Thin Solid Films **348**, 165 (1999).
[39] E. Çetinörgü, S. Goldsmith, and R. L. Boxman, J. Cryst. Growth **299**, 259 (2007).
[40] X. T. Hao, J. Ma, D. H. Zhang, T. L. Yang, H. L. Ma, Y. G. Yang, C. F. Cheng, and H. Huang, Appl. Surf. Sci. **183**, 137 (2001).
[41] R. Ghosh, D. Basak, and S. Fujihara, J. Appl. Phys. **96**, 2689 (2004).
[42] M. S. Tokumoto, A. Smith, C. V. Santilli, S. H. Pulcinelli, A. F. Craievich, E. Elkaim, A. Traverse, and V. Briois, Thin Solid Films **416**, 284 (2002).
[43] C. Lee, K. Lim, and J. Song, Sol. Energy Mater. Sol. Cells **43**, 37 (1996).
[44] D. C. Reynolds, D. C. Look, B. Jogai, J. E. Van Nostrand, R. Jones, and J. Jenny, Solid State Commun. **106**, 701 (1998).
[45] Y. C. Kong, D. P. Yu, B. Zhang, W. Fang, and S. Q. Feng, Appl. Phys. Lett. **78**, 407 (2001).
[46] K. Vanheusden, W. L. Warren, C. H. Seager, D. R. Tallant, J. A. Voigt, and B. E. Gnade, J. Appl. Phys. **79**, 7983 (1996).
[47] D. C. Look and B. Claflin, Phys. Status Solidi B **241**, 624 (2004).
[48] A. Janotti and C. G. Van de Walle, Appl. Phys. Lett. **87**, 122102 (2005).
[49] S. A. Studenikin, N. Golego, and M. Cocivera, J. Appl. Phys. **84**(4), 2287 (1998).
[50] V. Srikant and D. R. Clarke, J. Appl. Phys. **83**, 5447 (1998).
[51] L. N. Dem'yanets, L. E. Li, and T. G. Uvarova, J. Cryst. Growth **287**, 23 (2006).
[52] F. A. Selim, M. H. Weber, D. Solodovnikov, and K. G. Lynn, Phys. Rev. Lett. **99**, 085502 (2007).
[53] D. Wang, H. W. Seo, C.-C. Tin, M. J. Bozack, J. R. Williams, M. Park, N. Sathitsuksanoh, An-jen Cheng, and Y. H. Tzeng, J. Appl. Phys. **99**, 113509 (2006).
[54] D. H. Zhang, Z. Y. Xue, and Q. P. Wang, J. Phys. D **35**, 2837 (2002).
[55] B. J. Jin, S. Im, and S. Y. Lee, Thin Solid Films **366**, 107 (2000).
[56] S. Sakohara, L. D. Tickanen, and M. A. Anderson, J. Phys. Chem. **96**, 11086 (1992).
[57] G. H. Jonker, Solid State Electron. **7**, 895 (1964).
[58] A. van Dijken, E. A. Meulenkamp, D. Vanmaekelbergh, and A. Meijerink, J. Lumin. **90**, 123 (2000).
[59] J. D. Ye, S. L. Gu, F. Gi, S. M. Zhu, S. M. Liu, X. Zhou, W. Liu, L. Q. Hu, R. Zhang, Y. Shi, and Y. D. Zheng, Appl. Phys. A **81**, 759 (2005).
[60] Z.-M. Liao, H.-Z. Zhang, Y.-B. Zhou, J. Xu, J.-M. Zhang, and D.-P. Yu, Phys. Lett. A **372**, 4505 (2008).